



Extending Inverse Heat Conduction Method to Estimate Flight Trajectory of a Reentry Capsule

V. Tahmasbi¹ and S. Noori^{2,*}

Department of Aerospace Engineering, Amirkabir University of Technology, Tehran, Iran

ABSTRACT: This study is dedicated to the solution of the inverse heat conduction problem for estimation of the time-varying velocity and altitude profiles regarding the flight trajectory of an earth-entry capsule. Four tungsten-rhenium sensors are supposed to be embedded inside the ablative heat shield of the probe, three of which cannot tolerate high-temperature conditions and burn out during entry and the other one remained intact until the end of the simulation. The conventional Levenberg-Marquardt method is reinforced by a relaxation scheme to prevent unfavorable severe oscillations encountered in the inverse iterations. To keep the generality of the method, no prior knowledge on the thermal condition and surface recession of ablative insulator is utilized in the current estimation. Therefore, in the associated direct problem, velocity and altitude profiles are given and the temperature field inside the heat shield is determined. Accordingly, a solution of the direct problem consists of (i) bow shock calculations in dissociated air (ii) boundary layer solver to compute stagnation heating rate (iii) identification of the thermal response of charring ablative heat shield. It is shown that if the standard deviation of the temperature measurement error is 5 K, estimation of altitude and velocity are associated with approximately 10 and 5 percent normalized error,

Review History:

Received: Sep. 04, 2019

Revised: Dec. 25, 2019

Accepted: Dec. 29, 2019

Available Online: Jan. 04, 2020

Keywords:

Charring ablator

Inverse heat conduction problem

Flight trajectory

Reentry vehicle

1- Introduction

The simulation and ground tests' results for a space vehicle can differ significantly from the real situation occurring in flight missions. Therefore, different types of sensors were embedded to record flight data such as accelerations, pressure, and temperatures. A better analysis of the corresponding data, helps researchers to obtain comprehensive knowledge about real conditions which the vehicle experienced during flight. Among sensors, thermocouples have been widely used for acquiring temperatures during the flight missions. These time-varying temperatures were then used in the so-called Inverse Methods (IMs) to identify thermal conditions which the space vehicle experienced during flight such as conductive and radiative heat transferred to the body.

Inverse problems are classified as ill-posed problems and they are concerned with the determination of unknown causes from the given effects. Inverse Heat Conduction Problems (IHCPs) related to the estimation of parameters or functions (such as thermal conductivity, specific heat, boundary heat flux, wall temperature, etc.) by applying temperatures recorded by thermocouples that are located inside a solid medium. Some textbooks [1-3] and several articles [4-13] have so far addressed IHCP. Several computational schemes in IHCPs have been reviewed by Chang et al. [5]. They found that the present-day challenge in IHCPs is how to address the

complicated geometry. Thermal conductivity of porous media, with cylindrical and bullet shapes, was recently recovered using the inverse heat conduction method by Fabela et al. [6]. Conjugate Gradient Method (CGM) and a complex variable method were utilized in their work to estimate unknown properties. Bozzoli et al. [4] adopted inverse problem to predict the thermal conductivity of fire protective materials.

Accurate knowledge of surface heat flux is a crucial aspect in a wide variety of fields, which is why researchers tend to develop various inverse methods for specifying boundary heating load [7-13]. Inverse heat conduction methods have extensive application in the aerospace industries, especially for realizing aero-thermal environmental conditions of space vehicles during atmospheric reentry. These unknown thermal conditions (including surface heat flux, surface temperature, etc.) can be deduced inversely from time-wise temperatures measured by sensors that are placed in-depth of the heat shield. Ablative Thermal Protection Systems (TPSs) are commonly used as a heat shield barrier to protect reentry vehicles exposed to severe heat loads. Ablative materials are generally categorized into two classes. The first type is a non-charring ablator (e.g., graphite) which discharges energy from the material through surface recession caused by thermochemical reactions. The second is charring-ablator (e.g., carbon-phenolic composite) which discharges energy through both self-immolation (surface recession) and pyrolysis by which the virgin composite chemically

*Corresponding author's email: s_noori@aut.ac.ir



converts into char. Dowding et al. [14] estimated thermal properties, which are characterized by the quadratic function of temperature, and surface heat load of carbon-carbon composite for a temperature range of 30-600°C. Because of the low working temperatures in reference [14], the ablative material did not undergo chemical reaction and recession on the hot surface. Another study was conducted by Petrushevsky and Cohen [15] to estimate surface heat flux and recession. The threshold temperature of ablation was exceeded during their simulation and due to oxidation, surface phase change (recession) occurred. However, they installed sensors at the deep location from the receding surface to prevent damage to the sensors. Oliveira and Orlande [16] utilized measured temperatures and recession to conduct an inverse procedure for reconstructing surface heat flux of an ablator. Unlike the conventional least square norm, the modified objective function was defined in reference [16] to match both the measured temperature and surface position. Because of the ill-posed nature of IHCPs, two regularization techniques, including discrepancy principle and measurement filtering, were evaluated in reference [16] to stable the solution with respect to random errors. Estimation of boundary conditions for ablative materials can also be found in other research works [17-25].

Considering the aforementioned review of the articles, it is apparent that the inverse heat conduction technique has often been applied for the assessment of thermal boundary conditions and thermo-physical property of ablative materials. In the current work, a novel approach was conducted to evaluate the flight trajectory of a space vehicle, comprising both the velocity and altitude of an earth-entry capsule, by solving IHCP. According to the author's knowledge, this is the first time the inverse heat conduction method has been used to estimate the flight trajectory of an entry vehicle. Reconstruction of the reentry velocity and altitude of a capsule from measured temperatures, recorded by sensors, has not yet been taken into consideration in the published work. In conventional IHCPs, the direct solver is a subroutine by which the direct heat conduction problem is frequently solved during estimation. In the present study, the solution routine for the direct problem was extended to solve in-depth heat conduction problem coupling with hypersonic viscous shock layer.

Trajectory estimation of unmanned exploration vehicle employed on Rosetta/CNSR [26] mission, proposed by the European Space Agency (ESA), is used to assess the accuracy of the current method. Entry vehicle's fore-body is protected by ablative heat shield from overheating to maintain comet material in its initial state. Measured temperatures by sensors embedded along the stagnation fore-body (through-the-thickness of ablative heat shield) were used to recover time-varying velocity and altitude of return probe. Time-wise altitude and velocity of the capsule are provided for direct solver as input and temperatures at sensors' locations are returned as output. Therefore, three distinct serial solvers were used to solve the direct problem consisting of; 1) Specifying conditions ahead of the bow shock (altitude and velocity),

airflow conditions behind the shock wave were determined by applying mass, momentum and energy equations governing a steady-adiabatic flow without frictional effects. Due to high jumps occurring in temperature across the normal shock wave, the air was assumed to be a hot gas in chemical equilibrium and thus the state of the gas behind the shock was obtained in an iterative manner. Because of the thin shock layer created in hypersonic flows, calculated quantities behind the normal shock were considered as gas properties at the edge of the boundary layer in the stagnation region. 2) Given the flow properties at the outer edge of the boundary layer (obtained in the first part), a solution of chemically equilibrium flow at stagnation region proposed by Fay and Riddle [27], which is still in prevalent use among researchers, was applied to determine cold wall heat flux in dissociated gas. The formulation based on work done by Tauber-Sutton [28] was used to estimate stagnation radiative heat flux caused by a hot luminous zone that was enclosed between the shock wave and the body. 3) Having identified the convective and radiative heat input to the body, thermal response of heat shield was assessed by Charring Material Thermal Response and Ablation code (CMA), which was developed by Aerotherm Corporation in 1968 [29]. An elaborate version of CMA finite difference code was developed in the current study for simultaneously analyzing the ablative insulator and substructure which were made of carbon-phenolic composite and Reusable Surface Insulation tiles (RSI), respectively.

Inverse estimation of parameters for charring ablators often encounters some difficulties. Burning out of the sensors because of the high working temperatures that the ablator undergoes during the reentry, can be mentioned as one of these problems. To overcome this challenge, sensors must be located deeper inside the ablator. Although this plan prevents sensors from damage, it results in significant time lagging between changes in heat flux at hot surface and sensors' response. Owing to inherent high insulation behavior of ablative materials, this time lagging has been raised, and thus inverse estimation is faced with serious problems to achieve reasonable results. To resolve the foregoing obstacle in the present work, four sensors located at different points through-the-thickness of the ablator were devoted to taking temperatures, three of which burned out and the deepest one withstood until the end of the reentry. Because of the wide range of temperatures that the heat shield was subjected to, the temperature dependency of thermo-physical properties must be taken into consideration. This feature, as well as the surface recession of the ablator, enhanced the nonlinear nature of the IHCP. Hence, Levenberg-Marquardt Method (LMM), as a common iterative technique to solve nonlinear optimization problems, was utilized in the current study. In the function estimation framework for ablative material, especially in the neighborhood of a bad initial guess, undesirable fluctuations in the estimating function happens during the iteration process which is caused by burning out of the sensors. These oscillations can be extremely high and may lead to stopping inverse iterations. To fix this problem in the present study, conventional LMM is reinforced with a relaxation scheme to confine oscillations within a certain

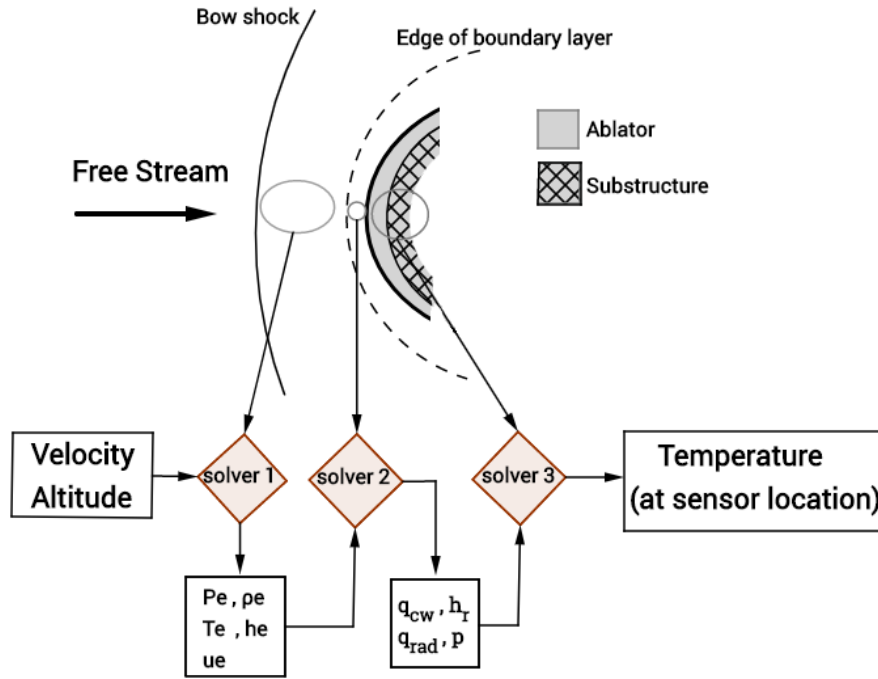


Fig. 1. Elements of direct solver and data exchange manner

limit. No prior information regarding the surface heat flux, the recession rate, etc. was utilized to keep the current estimation algorithm general. For further assessment of the proposed algorithm, the stability of the solution was investigated by adding random errors to the measurements.

2- Direct Problem

The so-called direct problem is concerned with the determination of the effects from the known causes which is categorized as well-posed. In this study, cause and effect were characterized by reentry trajectory (velocity and altitude) and temperature response through-the-thickness of the heat shield, respectively. In this fashion, three individual solvers were coupled to tackle the foregoing task. Data exchanged between solvers in a serial manner is shown in Fig. 1. Mathematical formulation regarding each solver will be stated in subsequent sections.

2-1- Flow properties at the boundary layer edge (solver 1)

Conservative equations that govern the flow passing through a normal shock wave can be given by the following relations:

Continuity :

$$\rho_{\infty} u_{\infty} = \rho_2 u_2 \Rightarrow u_2 = \frac{\rho_{\infty}}{\rho_2} u_{\infty} \quad (1)$$

Momentum :

$$p_{\infty} + \rho_{\infty} u_{\infty}^2 = p_2 + \rho_2 u_2^2 \Rightarrow \quad (2)$$

$$p_2 = p_{\infty} + \rho_{\infty} u_{\infty}^2 \left(1 - \frac{\rho_{\infty}}{\rho_2} \right)$$

Energy :

$$h_{\infty} + \frac{u_{\infty}^2}{2} = h_2 + \frac{u_2^2}{2} \Rightarrow \quad (3)$$

$$h_2 = h_{\infty} + \frac{u_{\infty}^2}{2} \left[1 - \left(\frac{\rho_{\infty}}{\rho_2} \right)^2 \right]$$

It is important to note that the above equations are valid for both reacting and frozen air. Thermodynamic properties ahead of the shock wave can be expressed in terms of altitude using the International Standard Atmosphere (ISA) model. Knowing the properties ahead of the shock wave, this system must be integrated by the following equations of state to calculate the five unknowns: $\tilde{n}_2, u_2, p_2, h_2$ and T_2 .

$$\rho_2 = \rho(p_2, T_2) \quad (4)$$

$$h_2 = h(p_2, T_2) \quad (5)$$

The normal shock wave that formed in front of the stagnation point was supposed to be intense enough. Therefore, the temperature behind the shock can be raised beyond the threshold temperature for vibrational excitation, dissociation and ionization, and hence calorically perfect gas cannot be a valid assumption for the air. In the situation of high-temperature equilibrium flow, Eqs. (1-5) must be solved numerically by an iterative process to yield reasonable results for the unknowns. The computational algorithm which was used in the current study can be summarized as follows:

Step 1: Suppose an initial value for \tilde{n}_2 according to the relation for the density behind the normal shock wave, in the

case of a perfect gas, as follows:

$$\rho_2 = \rho_\infty \frac{(\gamma + 1) M_\infty^2}{(\gamma - 1) M_\infty^2 + 2} \quad (6)$$

where γ is the ratio of specific heats and M_∞ is the free-stream Mach number.

Step 2: Having a value for \tilde{n}_2 , compute p_2 and h_2 from Eqs. (2) and (3).

Step 3: Compute T_2 from Eq. (5) using bisection method which is based on interval halving to find the approximate root of the functions.

Step 4: Compute \tilde{n}_2^{new} from Eq. (4) with the values of p_2 and h_2 just estimated.

Step 5: If the difference between density values (\tilde{n}_2 and \tilde{n}_2^{new}) becomes sufficiently small, stop iteration; otherwise, replace \tilde{n}_2 by \tilde{n}_2^{new} and return to step 2.

As shown above, despite analyzing shock wave in a calorically perfect gas, in which ratios of quantities through the shock are obtained explicitly by the free-stream Mach number, an iterative algorithm is required for the case of equilibrium gas to calculate these ratios as a function of free-stream velocity, pressure, and temperature. Eventually, because of the thin shock layer in hypersonic speeds, properties estimated behind the shock wave were considered for the edge of the boundary layer. It is noteworthy that thermodynamic properties of air in the chemical equilibrium tabulated by Hansen [30] are used to characterize equations of state (Eqs. (4) and (5)).

2-2- Stagnation-region heat transfer in dissociating air (solver 2)

In this section, our attention is dedicated to the estimation of convective and radiative stagnation point heat flux. The powerful correlation proposed by Fay and Riddle [27] aggregated from numerous boundary layer solutions was used to compute convective cold wall heat flux in chemical equilibrium state as

$$q_{cw} = 0.76 Pr^{-0.6} (\rho_e \mu_e)^{0.4} (\rho_w \mu_w)^{0.1} \sqrt{\left(\frac{du_e}{dx}\right)_s} (h_{0e} - h_w) \left[1 + (Le^{0.52} - 1) \left(\frac{h_D}{h_{0e}}\right) \right] \quad (7)$$

where h_D is the chemical enthalpy of gas at the edge of the boundary layer and defined by

$$h_D = \sum_i c_{i_e} (\Delta h_f)_i^o \quad (8)$$

Velocity gradient at stagnation region was approximated by Newtonian law as follows:

$$\left(\frac{du_e}{dx}\right)_s = \frac{1}{R} \sqrt{\frac{2(p_e - p_\infty)}{\rho_e}} \quad (9)$$

Properties at the edge of the boundary layer (provided in the previous section) were employed in Eq. (7) to compute cold wall heat flux.

Radiative heat load transferred from the hot luminous shock layer zone to the reentry capsules can be large enough as well as the convective heat flux. One of the popular correlations to calculate radiative heat flux at the stagnation region of reentry vehicles was accomplished by Tauber and Sutton [28] for thermochemical equilibrium conditions. They found that radiative heating for the earth's atmosphere can be expressed by the following general relation:

$$q_{rad} = C R_n^a \rho_\infty^b f(u_\infty) \quad (10)$$

where b and C are constants and a depends on the free stream density, velocity, and nose radius. These coefficients as well as $f(u_\infty)$, which is a tabulated function of free stream velocity, are given in detail by Tauber [28]. Notice that the radiative correlation is only affected by the free-stream properties and the estimated quantities in the previous section do not play any role in the current formulation.

Two required parameters which must be stated, before thermal processing in the next section begins, are the recovery enthalpy and pressure. Gas pressure at the wall was considered the same as that of the boundary layer edge. The exact determination of recovery enthalpy (or enthalpy of the adiabatic wall), is achieved by numerical solution of boundary layer equations under the adiabatic wall condition along the vehicle's trajectory. However, in the practical purposes, h_r is represented in terms of boundary layer edge properties and recovery factor by:

$$h_r = h_e + r \frac{u_e^2}{2} \quad (11)$$

where r is the recovery factor and can be approximated by $(Pr)^{1/2}$ and $(Pr)^{1/3}$ for laminar and turbulent flow, respectively.

2-3- In-depth thermal response of heat shield (solver 3)

The in-depth thermal response of the ablator under intended thermodynamic and aeroheating conditions (predetermined in the latter part), was numerically predicted using an in-house CMA code, first developed by Aerotherm Corporation [29]. Thermal behavior of charring ablators is characterized by conservation of solid density and energy equations as follows:

$$Mass : \quad \nabla \cdot \dot{m}_g = -\frac{\partial \rho}{\partial t} \quad (12)$$

$$Energy : \quad \rho C_p(T) \frac{\partial T}{\partial t} = \nabla \cdot (k(T) \nabla T) - (h_g - \bar{h}) \nabla \cdot \dot{m}_g - \dot{m}_g \cdot \nabla h_g + (\rho C_p(T)) \dot{S} \cdot \nabla T \quad (13)$$

In the above Eqs. (12) and (13), the terms ρ , C_p , T , t , k , h_g , \dot{m}_g and \dot{S} respectively represent solid density, the specific heat of ablator, temperature, time, thermal conductivity, enthalpy of the pyrolysis gas, mass flux of the pyrolysis gas and surface recession rate of ablator. The physical meaning of Eq. (12) is that the net mass flux of pyrolysis gas, convected into the element, equals the mass of pyrolysis gas generated inside the element due to material decomposition. The terms in the energy equation from left to right can be separately interpreted as; accumulation rate of sensible energy, energy transferred by conduction, the rate of energy consumed by chemical reactions, energy convected by transmission of pyrolysis gas, and convection of sensible energy caused by the moving coordinate system. \bar{h} is a temperature-dependent quantity and it is defined by the following relationship:

$$\bar{h} = \frac{\rho_v h_v - \rho_c h_c}{\rho_v - \rho_c} \quad (14)$$

where indices “c” and “v” represent char and virgin state of the composite. After discretization, Energy conservation equations, for the i^{th} node, can be written as

$$A_i T_{i-1} + B_i T_i + C_i T_{i+1} = D_i \quad (15)$$

The coefficients A_i , B_i , C_i and D_i were determined by the following equations.

$$A_i = -\frac{\Delta t}{\Delta x_i} \frac{1}{\left[\frac{\Delta x_{i-1}}{2k_{i-1}} + \frac{\Delta x_i}{2k_i} \right]} \quad (16)$$

$$B_i = (\rho C_p)_i - \frac{\Delta t}{\Delta x_i} \frac{1}{\left[\frac{\Delta x_{i-1}}{2k_{i-1}} + \frac{\Delta x_i}{2k_i} \right]} + \frac{\Delta t}{\Delta x_i} \frac{1}{\left[\frac{\Delta x_i}{2k_i} + \frac{\Delta x_{i+1}}{2k_{i+1}} \right]} - \left(\frac{\partial h_g}{\partial T} \right)_i \left(\frac{\partial \rho}{\partial t} \right)_i \Delta t + \quad (17)$$

$$\frac{\dot{m}_{g_i}}{\Delta x_i} \left(\frac{\partial h_g}{\partial T} \right)_i \Delta t + \frac{\dot{S} \Delta t}{\Delta x_i} (\rho C_p)_i$$

$$C_i = -\frac{\Delta t}{\Delta x_i} \frac{1}{\left[\frac{\Delta x_i}{2k_i} + \frac{\Delta x_{i+1}}{2k_{i+1}} \right]} - \quad (18)$$

$$\frac{\dot{m}_{g_i}}{\Delta x_i} \left(\frac{\partial h_g}{\partial T} \right)_{i+1} \Delta t - \frac{\dot{S} \Delta t}{\Delta x_i} (\rho C_p)_{i+1}$$

$$D_i = T_i^{old} \left[\left(\rho C_p \right)_i - \left(\frac{\partial h_g}{\partial T} \right)_i \left(\frac{\partial \rho}{\partial t} \right)_i \Delta t + \frac{\dot{m}_{g_i}}{\Delta x_i} \left(\frac{\partial h_g}{\partial T} \right)_i \Delta t + \frac{\dot{S} \Delta t}{\Delta x_i} (\rho C_p)_i \right] + T_{i+1}^{old} \left[-\frac{\dot{m}_{g_i}}{\Delta x_i} \left(\frac{\partial h_g}{\partial T} \right)_i \Delta t - \frac{\dot{S} \Delta t}{\Delta x_i} (\rho C_p)_i \right] + \Delta t \left[h_{g_i} \left(\frac{\partial \rho}{\partial t} \right)_i - \bar{h}_i \left(\frac{\Delta \rho}{\Delta t} \right)_i + \frac{\dot{m}_{g_i}}{\Delta x_i} (h_{g_{i+1}} - h_{g_i}) + \frac{\dot{S}}{\Delta x_i} ((\rho h)_{i+1} - (\rho h)_i) \right] \quad (19)$$

The term $\left(\frac{\partial \rho}{\partial t} \right)$ which appears in the mass and energy balance equations is the decomposition rate of the ablator and demonstrates the chemical conversion rate of virgin material into complete char. For carbon-phenolic material, which we assume to be composed of three constituents, the decomposition rate for each of the three components can be formulated based on Arrhenius type of kinetic reaction expression. Accordingly, the density change rate for the individual material components and overall composite density can be represented by the following equations.

$$\frac{\partial \rho_j}{\partial t} = -A_j e^{-E_j/RT} \rho_{vj} \left(\frac{\rho_j - \rho_{cj}}{\rho_{vj}} \right)^{n_j} \quad (20)$$

$$j = B, C, D$$

$$\rho = \Gamma (\rho_B + \rho_C) + (1 - \Gamma) \rho_D \quad (21)$$

where A is the pre-exponential coefficient, E is the activation energy for decomposition, Γ is the volumetric fraction of resin in the virgin plastic which was nominally set to 0.4 for carbon-phenolic, B and C are the constituents of resin and D denotes the reinforcement. So the nodal density change $\left(\frac{\Delta \rho}{\Delta t} \right)$ can be determined by

$$\left(\frac{\Delta \rho}{\Delta t} \right)_i = \left(\frac{\partial \rho}{\partial t} \right)_i + \dot{S} \left(\frac{\Delta \rho}{\Delta x} \right) \quad (22)$$

The boundary condition at the ablative surface (hot surface) of the insulator was satisfied by specifying the Surface Energy Balance (SEB). The SEB equation can be derived from balancing the convection, radiation, conduction, and the energy interchanged between the solid surface and boundary layer due to chemical interactions. This equation, under the assumption of a unity Lewis and Prandtl numbers, can be written as

$$\frac{q_{cw} \phi_{blowing}}{h_r} \left[\begin{matrix} (h_r - h_w) + B'_c(h_c - h_w) + \\ B'_g(h_g - h_w) \end{matrix} \right] + \alpha q_{rad} - \varepsilon \sigma T_w^4 + \left(k \frac{\partial T}{\partial x} \right)_w = 0 \quad (23)$$

where $\phi_{blowing}$ is the blowing correction of cold wall heat flux, h_w is the enthalpy of the gas mixture adjacent to the wall, B'_g and B'_c are non-dimensional pyrolysis and char mass fluxes at the surface. In the above Eq.(23), q_{cw} , h_r and q_{rad} are known from the previous section. B'_g is also delivered by the solution of the mass equation. The last term in Eq. (23) represents conductive heat flux which connects the SEB to the in-depth thermal solution (Eq. (13)). Rearranging the tri-diagonal matrix, obtained from the discretization of Eq. (13), resulted in finding conductive heat flux as a linear function of surface temperature. Since there are two unknowns in Eq. (23) (B'_c and T_w) and only one equation, an auxiliary problem is demanded to relate char mass flux and wall temperature. This can be accomplished by using Aerotherm Chemical Equilibrium (ACE) code to generate the desired surface thermochemical Tables. The in-depth thermal solver has much more details, such as grid generation scheme, moving mesh algorithm, and coupling strategy between mass and energy equations, which are ignored to save space. For more information on CMA, the reader can refer to the original technical report [29].

3- Inverse Problem

The IHCP was extended to the estimation of velocity and altitude of a reentry capsule from temperature values taken by the sensors which were located through-the-thickness of the heat shield. Owing to the strongly non-linear nature of the problem, the LMM as a powerful iterative technique was chosen to minimize the following least-square norm.

$$S(\mathbf{X}) = \sum_{m=1}^M \sum_{n=1}^N [Y_{nm} - T_{nm}(\mathbf{X})]^2 \quad (24)$$

where M and N indicate the number of sensors and number of temperature measurements per individual sensor. Y_{nm} are the measured temperatures and T_{nm} are estimated temperatures at sensors' locations achieved by solving the direct problem. \mathbf{X} represents the vector of unknown parameters which was substituted by the time-functional form of velocity or altitude in the current study. New estimates in the iterative procedure of the LMM to minimize the objective function $S(\mathbf{X})$, Regardless of the mathematical proof, can be given by [3]:

$$\mathbf{X}^{i+1} = \mathbf{X}^i + \left[(\mathbf{J}^i)^T \mathbf{J} + \mu^i \Psi^i \right]^{-1} (\mathbf{J}^i)^T [\mathbf{Y} - \mathbf{T}(\mathbf{X}^i)] \quad (25)$$

where Ψ is a diagonal matrix involving the diagonal elements of $[\mathbf{J}^T \mathbf{J}]$ and J is the Jacobian matrix defined as first-order partial derivatives of temperatures with respect to the unknown parameters. By this definition, elements of the Jacobian matrix in the case of multiple sensor readings can be given by

$$J_{kj} = \frac{\partial T_{nm}}{\partial X_j} \quad \text{for} \quad \begin{cases} n = 1, \dots, N \\ m = 1, \dots, M \\ j = 1, \dots, J \end{cases} \quad (26)$$

where J refers to the number of unknown parameters and index k is the row number of the Jacobian matrix which is related to the measurement number n and sensor number m by the following

$$k = (m - 1)N + n \quad (27)$$

It is important to note that due to the burning out of the sensors during operation, the value of N may be different for different sensors. The parameter μ in Eq. (25) is a scalar damping factor. This parameter has a large value at the beginning of the iteration process and therefore LMM is inclined to the Steepest Descent Method (SDM). However, as the iteration progresses the damping factor is reduced gradually, and consequently, LMM behaves as Gaussian Method (GM). Hence, the self-adjustment damping parameter used in LMM, regularizes the inverse solution against the random errors.

In the inverse estimation, the sensitivity of temperatures at sensors' locations with respect to some parameters (for example velocity at certain times in current work), can be significantly smaller than the sensitivity for other parameters. So, in the beginning of the inverse iterations, drastic oscillations may be revealed in such parameters. But these oscillations do not appear to be problematic in the conventional IHCPs. Because by advancing iterations, these fluctuations are damped and exact values are recovered for the vector of estimated parameters (for the case of free-noise measurements). But, these undesirable oscillations can stop the inverse iteration procedure used in the current work. This problem has occurred because our direct solver routine cannot return the intended output when the exceedingly high increase in the value of estimating parameters happens. As an example, when these oscillations lead to extremely high values for altitude, standard atmosphere model used in direct solver cannot calculate thermodynamic properties ahead of the shock wave. Another case can be detected when a very high increment is exhibited in the estimated velocity values which results in high cold wall heat flux obtained by the Fay-Riddle approach. So, due to high heat flux exerted to the surface, the heat shield is fully ablated and CMA solver cannot return the temperatures at sensors' locations. To overcome this obstacle, the variation of unknown parameters during the iterative estimation can be confined within certain

limits (e.g., limiting the velocity with an upper bound of 20 km/s during iterations). To do so, a priori knowledge on the maximum amplitude of velocity and altitude of the capsule is demanded. But, knowing a priori information on the unknown parameters, distorts the general applicability of inverse methods. Molavi et al. [31] updated a conventional LMM by multiplying the search direction by a constant scalar interpolation factor as

$$\mathbf{X}^{i+1} = \mathbf{X}^i + \lambda \Delta \mathbf{X}^i \quad (28)$$

The search step size of all estimated parameters is relaxed by using this modification and hence cannot remove the aforementioned difficulty. Because oscillation amplitude of parameters with smaller sensitivity cannot be damped until other parameters, which have larger sensitivity coefficients, adequately approach their exact values. So, LMM was powered by a non-constant relaxation factor, as following to hold the vector of estimated parameters in an acceptable range.

$$\lambda = \begin{cases} \beta & \text{if } |\Delta \mathbf{X}^i| \geq \beta |\mathbf{X}^i| \\ 1 & \text{if } |\Delta \mathbf{X}^i| < \beta |\mathbf{X}^i| \end{cases} \quad (29)$$

where β is a positive constant factor which is set to 0.1 in the present work. In the current approach, parameters with small increments during iteration were not restricted and were allowed to advance forward freely to the final solution.

With these explanations, the computational algorithm for LMM can be summarized as follows:

Step 1: Set values of 0.001 and 0 for μ^i and i , respectively. Provide the vector of temperature measurements \mathbf{Y} , initiate the vector of unknown parameters \mathbf{X}^i and go to the next step.

Step 2: Solve the direct problem using known estimate of \mathbf{X}^i to obtain a vector of estimated temperatures $\mathbf{T}(\mathbf{X}^i)$ and then compute objective function $\mathcal{S}(\mathbf{X}^i)$ from Eq. (24).

Step 3: Compute the Jacobian matrix \mathbf{J}^i whose elements are presented in Eq. (26) and next determine the diagonal matrix Ψ^i .

Step 4: Solve the following linear system of equations by an arbitrary method (Cholesky factorization method used in the current study) to compute $\Delta \mathbf{X}^i$:

$$\begin{aligned} [(\mathbf{J}^i)^T \mathbf{J}^i + \mu^i \Psi^i] \Delta \mathbf{X}^i = \\ (\mathbf{J}^i)^T [\mathbf{Y} - \mathbf{T}(\mathbf{X}^i)] \end{aligned} \quad (30)$$

Then, determine the new vector of estimates from Eqs. (28) and (29).

Step 5: Given the new vector of estimates \mathbf{X}^{i+1} , solve the direct problem in order to obtain new estimated temperatures $\mathbf{T}(\mathbf{X}^{i+1})$ and afterward compute objective function $\mathcal{S}(\mathbf{X}^{i+1})$ from Eq. (24).

Step 6: If $\mathcal{S}(\mathbf{X}^{i+1}) > \mathcal{S}(\mathbf{X}^i)$, set $\mu^i = 10\mu^i$ and go back to step 4.

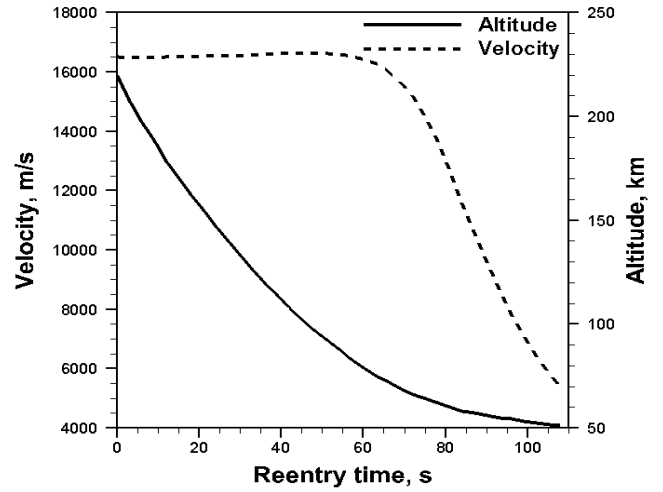


Fig. 2. Velocity and altitude of the probe versus time

Step 7: If $\mathcal{S}(\mathbf{X}^{i+1}) < \mathcal{S}(\mathbf{X}^i)$, accept the new vector of estimates \mathbf{X}^{i+1} , set $\mu^i = 0.1\mu^i$ and proceed to the next step.

Step 8: Stop the iterative procedure if the stopping criterion is satisfied based on the discrepancy principle as:

$$\mathcal{S}(\mathbf{X}^{i+1}) < \varepsilon \quad (31)$$

Otherwise, replace i by $i+1$ and return to step 3.

In the case of free-noise measurements, tolerance ε was chosen as enough small number to ensure that the value of objective function tended toward the expected minimum value of zero. For noisy data, an appropriate value was selected ε so that the difference between the measured and estimated temperatures was reduced on the order of standard deviation of the measurements in order to make sure a stable solution is achieved, as follows:

$$\varepsilon = \sum_{m=1}^M \sum_{n=1}^N [\sigma_{nm}]^2 = \sigma^2 \sum_{m=1}^M N_m \quad (32)$$

where σ_{nm} represents the standard deviation of measurement error which is assumed to be constant. N_m is the number of measurements recorded by sensor number m which is not an identical value for all of the sensors; because of the burning out of the sensors during atmospheric entry.

4- Results and Discussion

In this section, in order to examine the capability of the proposed inverse strategy, the trajectory of the entry probe used in Rosetta/CNSR mission (proposed by ESA in collaboration with NASA) was estimated. In this regard, velocity and altitude profiles of the probe before parachute deployment and during elapsed entry time of 108s, are depicted in Fig. 2.

The capsule was insulated in the stagnation region from high ambient temperature by an ablator made of a carbon-phenolic composite of thickness 28 mm and a backup reusable insulator comprised of LI-900 tile material of thickness 50

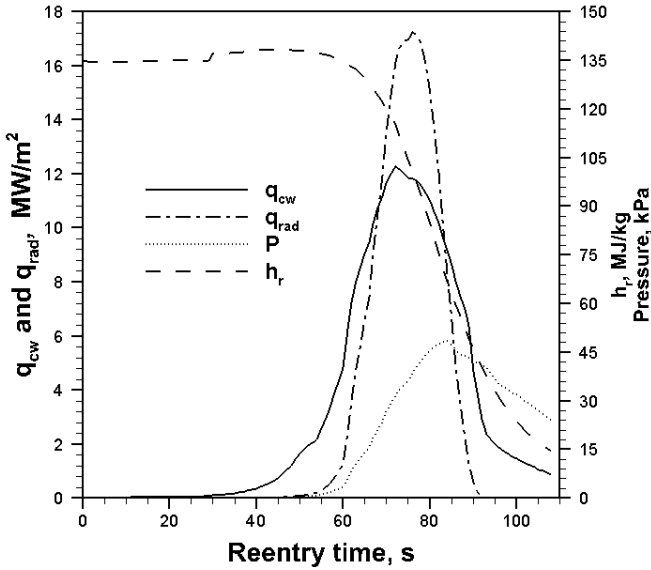


Fig. 3. Aerodynamic and thermal Environmental conditions at stagnation region

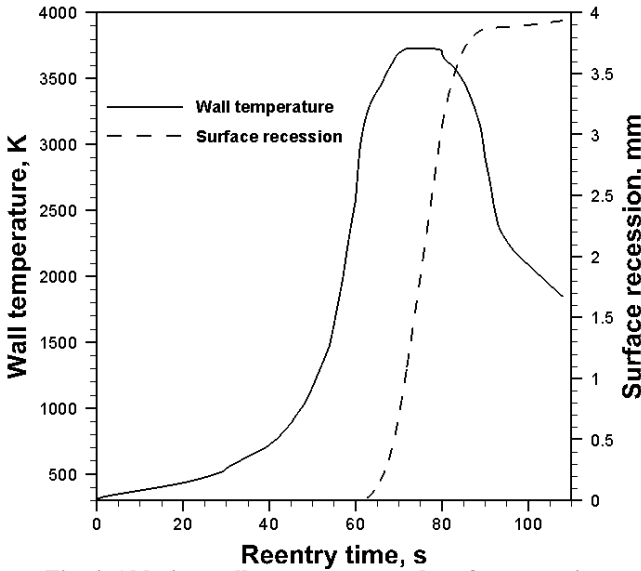


Fig. 4. Ablative wall temperature and surface recession

mm. Kinetic and thermo-physical coefficients of carbon-phenolic material and thermophysical properties of LI-900 low-density reusable insulator were taken from [32] and [33], respectively. Choosing appropriate time steps and grid sizing for CMA were performed Based on the experience gained in the current study and some basic primary rules provided in [34] to avoid instabilities and achieve adequate precision. Accordingly, 400 and 50 nodes were applied to discretize the carbon-phenolic and backup structure, and the value of 0.01s was taken as the time step size.

Given the exact profiles of the velocity and the altitude, environmental and surface thermal conditions comprising cold wall heat flux, radiation heat flux, recovery enthalpy, pressure, wall temperature, and surface recession were obtained from the solution of the direct problem and plotted versus entry time in Figs. 3 and 4. As shown in Fig. 3, the

capsule was subjected to severe radiative and convective pulse-heating in which radiative heat transfer exceeded convective flux at high entry speeds. It should be noted that these conditions are regarded as unknown functions, to be determined through the current inverse estimation.

In the current estimation approach, it is assumed that four thermocouples were embedded inside the carbon-phenolic heat shield at distances of 1mm, 3mm, 4mm, and 6mm from the initial location of the ablative surface at the stagnation point, as shown in Fig. 5. Knowing the exact prior values of the velocity and altitude (Fig. 2), measured temperatures were simulated by the solution of the direct problem at sensor positions. Also, it is assumed that all of the temperature measurements are made by tungsten-rhenium thermocouples which can tolerate high temperatures up to 2500 K. According to the sensor restrictions for data recording, the time interval between temperature measurements taken by each sensor was assumed to be 0.5s. Figure 6 illustrates the measured temperatures made by four individual sensors up to the elapsed time of 108s. Subsequently, it is evident that the three shallower sensors (Nos. 1,2,3) burned out at elapsed times of 66s, 77s, and 82s, respectively; and the deepest one (No. 4) was not demolished and withstood until the desired time of 108s.

From Fig. 6, estimation of the unknown parameters seems to be feasible over the whole time domain with a single sensor located at depth of 6mm. However, using a single sensor to reconstruct parameters, current estimation faced with serious difficulties regarding linear-dependency among the columns of the Jacobian matrix. The alleviation of this difficulty was achieved by using four sensors for reading temperatures. To show this fact, correlation coefficients between estimated parameters, which is defined as the covariance of the unknown parameters divided by their standard deviations, were computed as [3]

$$[R]_{ij} = \frac{cov(X_i, X_j)}{(\sigma_{X_i})(\sigma_{X_j})} = \frac{[J^T J]_{ij}^{-1}}{\sqrt{[J^T J]_{ii}^{-1}} \times \sqrt{[J^T J]_{jj}^{-1}}} \quad i, j = 1, \dots, J \quad (33)$$

where σ_{X_i} is the standard deviation of the estimated parameter X_i . By this definition, correlation coefficients can be assigned values in the range [-1,1], in which larger absolute values depict a stronger link amongst estimated parameters. Figures 7 (a) and (b) show the elements of the calculated correlation matrix in the case of velocity estimation for the two arrangements of single and quad-sensor. For further assessment, a semi correlation time interval was defined as the halftime range in which individual velocity components took zero correlation coefficients with the neighboring velocities. In other words, for each velocity component, a time range demanded to move forward or backward in time

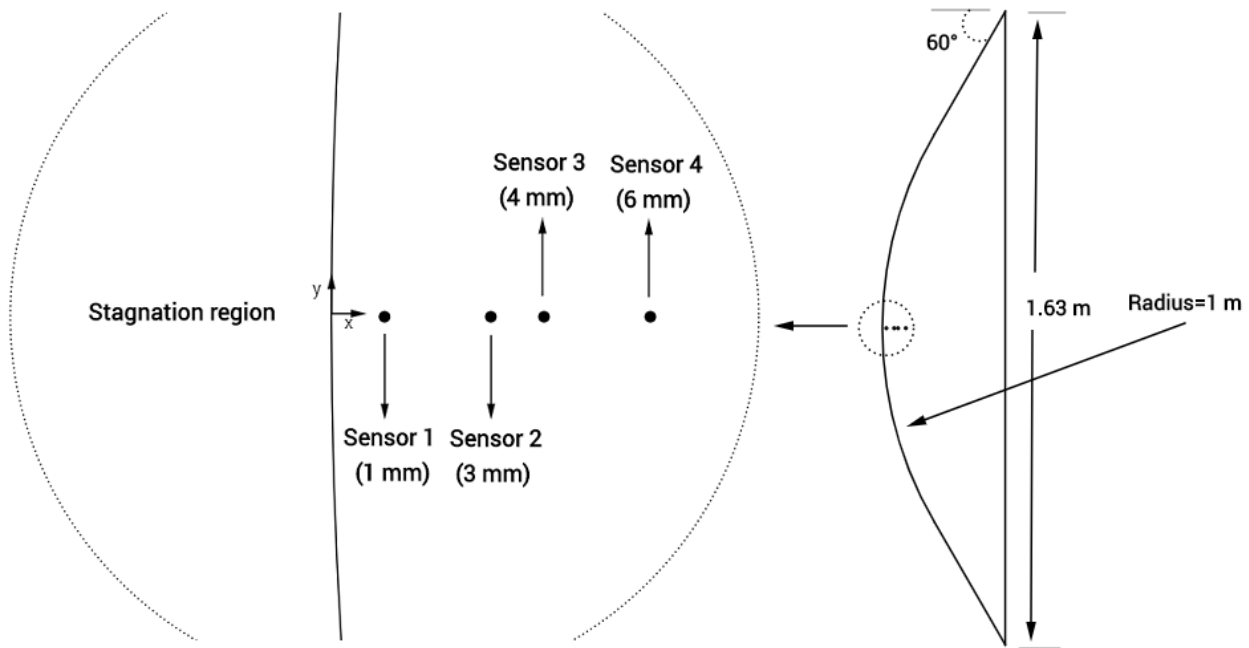


Fig. 5. Sensors' configuration through-the-thickness of the probe heat shield

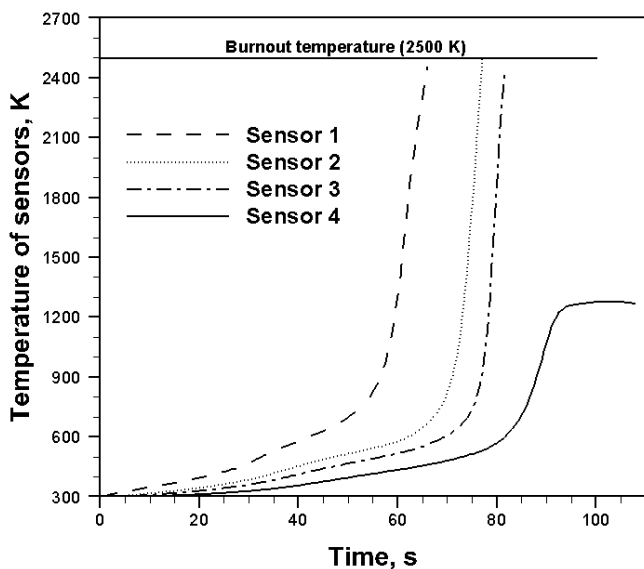


Fig. 6. Simulated sensors' temperature used to recover velocity and altitude

in order to find uncorrelated velocity which was specified as semi correlation time interval. As apparent from Fig. 7, the mean value for correlation time-bound interval was roughly reduced from 21s to 12s by increasing the number of sensors.

In the following sections, we describe the estimation results obtained with such measurement setup involving the number and location of sensors and time step between temperature readings by sensors. Profiles of the velocity and altitude were recovered every three seconds during entry time. Note that the velocity and altitude were estimated separately and indeed the estimation of individual unknown function (velocity or altitude) was performed using already associated exact values

for another function.

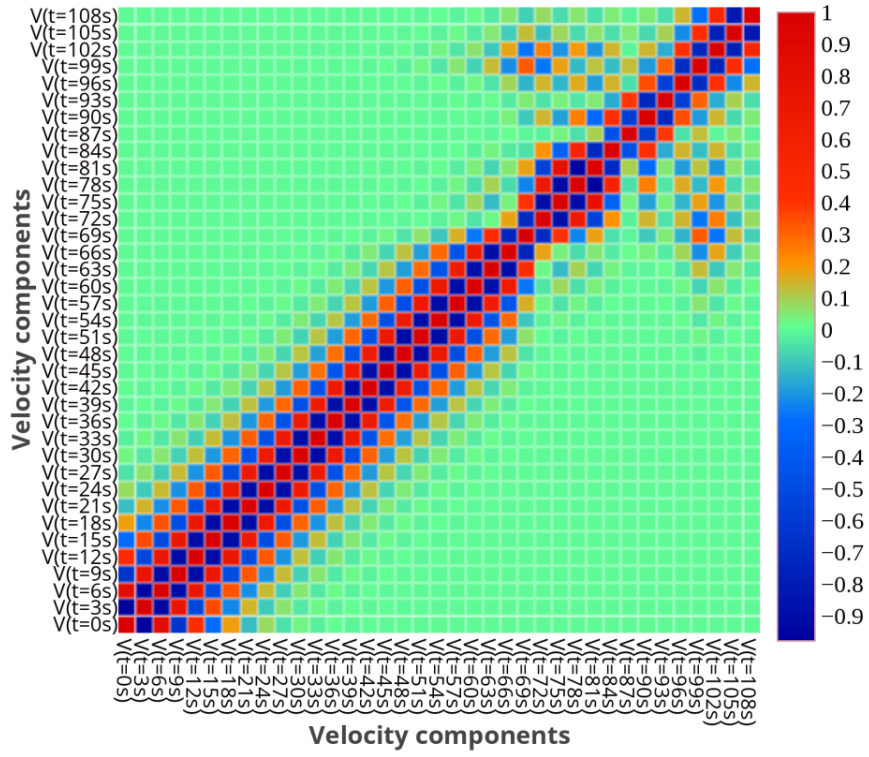
4-1- Velocity estimation

Estimation results of the recovering velocity are presented in the current section. A bad initial guess of 10 km/s was chosen in the iterative procedure to demonstrate the capability of the current method to resolve instabilities due to the ill-conditioned nature of the inverse problem near the initial guess at the beginning of iterations. Three types of data were utilized in the present estimation: 1) Noise-free measured temperatures for evaluation of inverse technique in order to predict sufficiently accurate estimates; 2) Noisy temperature of sensors in order to check whether the current estimation approach is stable with respect to errors in the measured data; 3) Existing error in pre-measured (or computed) altitude profile.

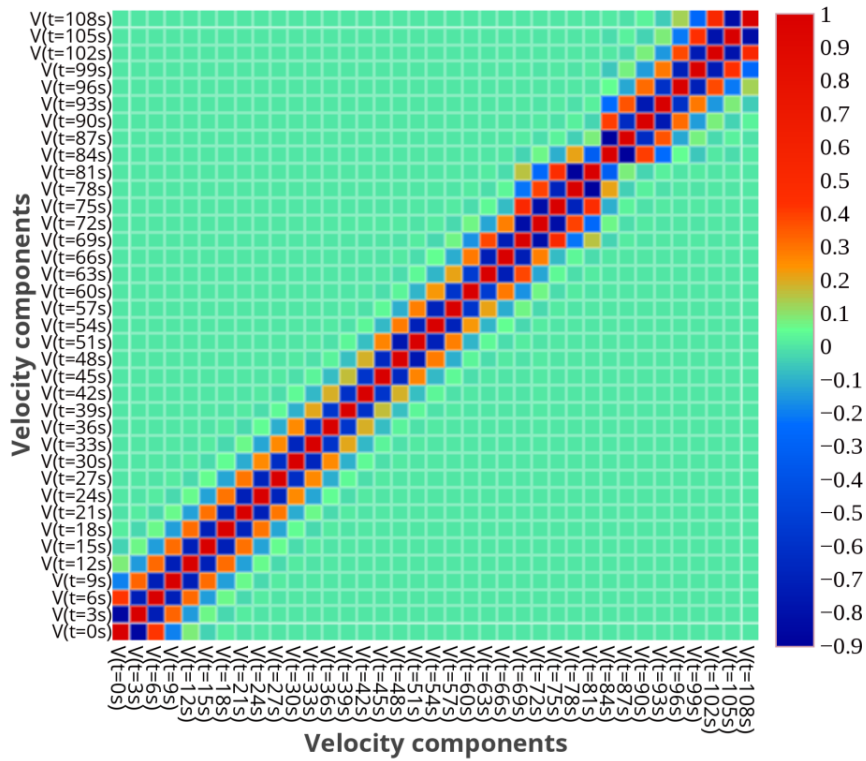
As illustrated in Fig. 8, estimation of velocity in absence of noise led to adequately precise results. For stability assessment of solution with respect to the errors in temperature measurements, exact temperatures were perturbed by random errors having normal probability distributions with zero means and standard deviations of 5K and 10K as follows:

$$Y^{(noisy)} = Y^{(exact)} + \eta\sigma \quad (34)$$

where σ is the standard deviation of the error in the measured temperatures and η is a random number generated in range $[-2.576, 2.576]$ for 99% confidence level. Figures (9) and (10) display corresponding velocity estimations belonging to noisy temperatures with $\sigma = 5K$ and $\sigma = 20K$, respectively. Dashed-lines in both Figures show the confidence intervals for the estimated velocity, which were computed statistically



(a)



(b)

Fig. 7. (a) Correlation matrix for single-sensor placement strategy (b) Correlation matrix for quad-sensor placement strategy

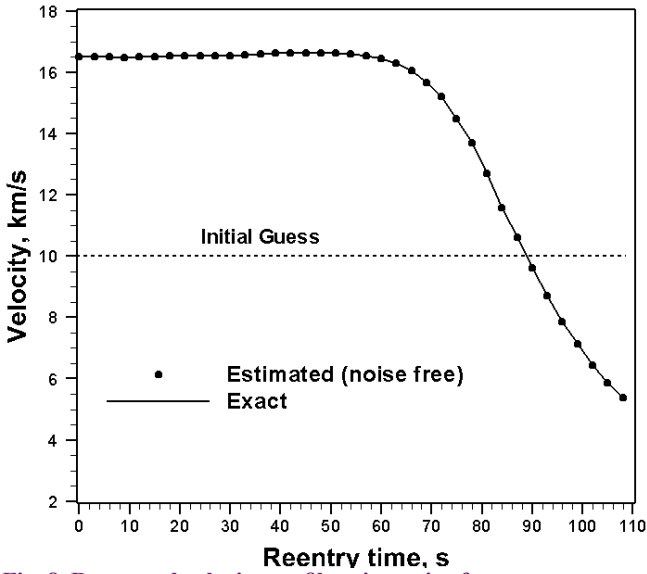


Fig. 8. Recovered velocity profile using noise-free measurements

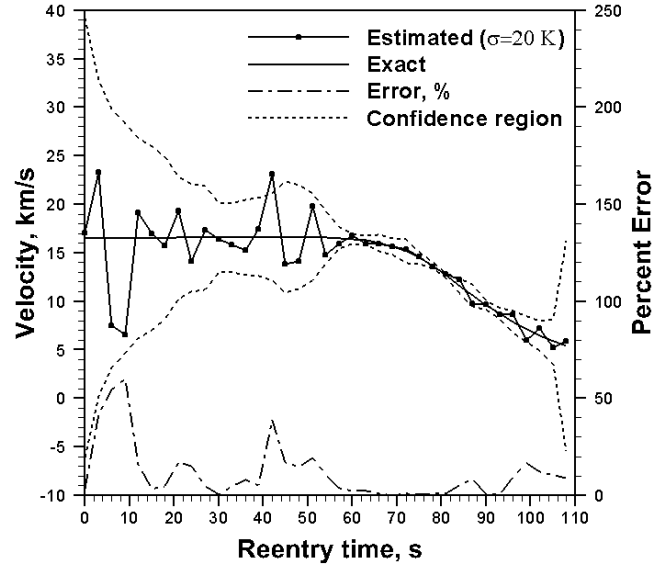


Fig. 10. Retrieved velocity profile using noisy measured temperatures ($\sigma = 20K$)

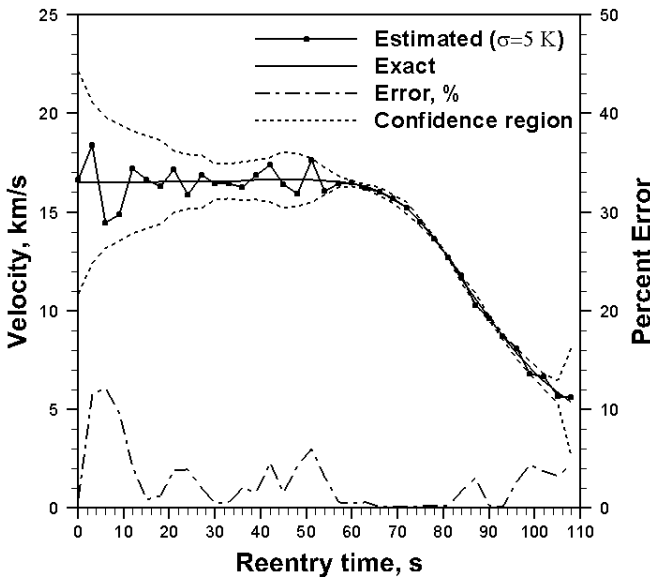


Fig. 9. Retrieved velocity profile using noisy measured temperatures ($\sigma = 5K$)

as follows before the inverse estimation procedure came into the beginning.

$$\begin{aligned} X_i^{exact} - 2.576 \sigma_{X_i} &\leq X_i^{estimated} \\ &\leq X_i^{exact} + 2.576 \sigma_{X_i} \end{aligned} \quad (35)$$

$$\sigma_{X_i} = \sigma \sqrt{[J^T J]_{ii}^{-1}} \quad i = 1, \dots, J \quad (36)$$

where $\hat{\sigma}_{X_i}$ represents the standard deviation of estimated velocity components (or altitude components in the next

section). As shown in these Figures, the velocity components were estimated within confidence intervals except for the case of $\sigma = 20K$ an entry time of 42s. The confidence region is approximately achieved for each velocity component without taking into consideration the estimation of other components, which may be why the estimation transgressed predestined confidence interval at this time. As observed in Figs. (9) and (10), estimations oscillated around the exact profile of velocity in the first 55s of entry. This can be due to small radiative and convective heat fluxes which have occurred because of the low density of air associated with high altitudes in this time interval (Fig. 3). This leads to a much smaller sensitivity of in-depth temperatures with respect to changes in the velocity components in the first 55s compared to later entry time points.

As another test case, effects of error in outlined altitude profile on the retrieved velocity profile were examined. Thus, the exact profile of altitude was perturbed by random errors with maximum values of $\pm 0.01H_{max}$ ($H_{max} = 220km$ based on Fig. 2). This situation can be achieved if the standard deviation is set to the value of 854.03m in Eq. (28). Note that the inverse problem was solved using errorless temperatures in this case. This is because the discrepancies between the exact and estimated velocities caused by errors in altitude profile can be distinguished from the estimation errors that occur due to existing noise in the temperatures. Fig. 11 presents the exact and estimated velocity profile for this test case. As can be seen, the estimated profile deviated from exact values in the time range from the 30s to 70s and near the end of entry time. These oscillations happened at different times compared to those in the previous case including noisy temperatures.

Fig. 12 demonstrates the decreasing histories in the objective function for inverse iterations regarding three test cases. As expected, a smaller amount of objective function for the standard deviation of 5K was achieved than that of

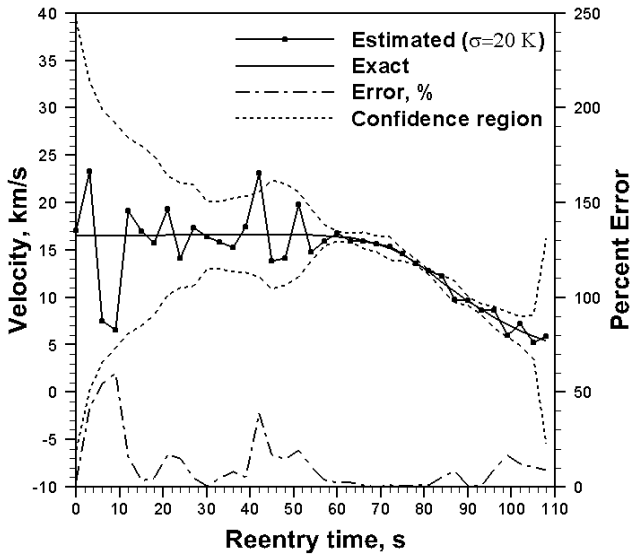


Fig. 11. Retrieved velocity profile using noisy altitude ($\sigma = 854.03\text{m}$)

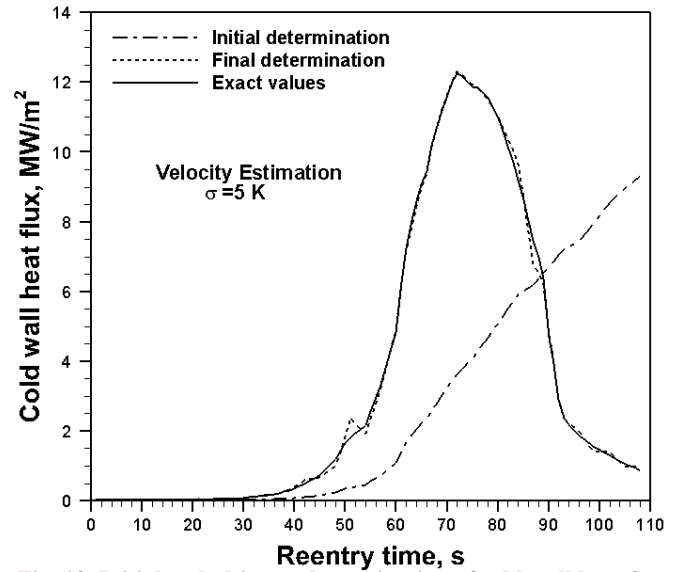


Fig. 13. Initial and ultimate determination of cold wall heat flux

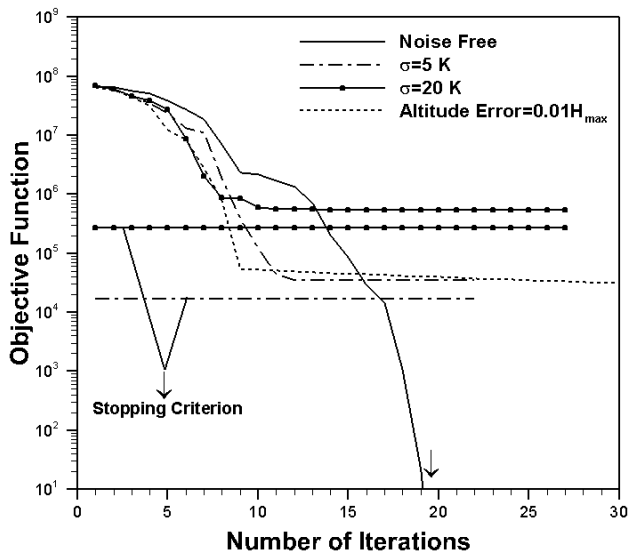


Fig. 12. The values of objective function versus iteration number in case of velocity estimation

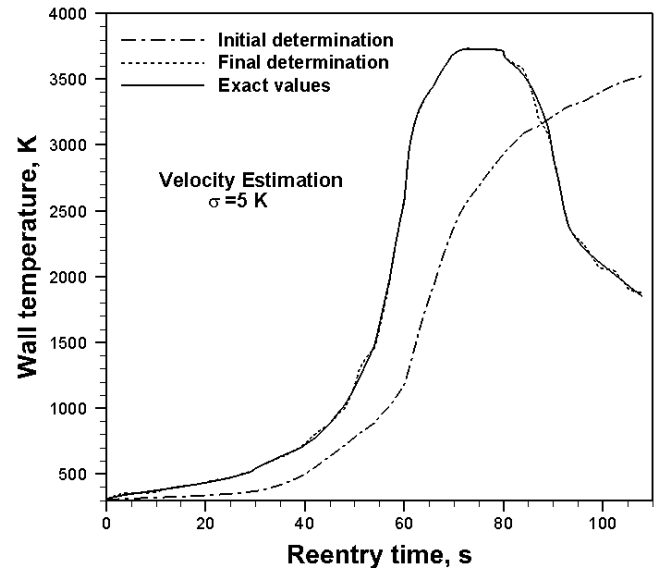


Fig. 14. Initial and ultimate determination of wall temperature

20K. Also, LMM automatically kept the amount of objective functions fixed in values slightly higher than those specified by the discrepancy principle in Eq. (26) confirming the inherent stability of LMM through the self-adjustment of damping factor μ in Eq. (25).

As previously mentioned, no prior information on the cold wall heat flux, wall temperature, and surface recession was available and these quantities were determined during the minimization of the objective function. The outcomes of such determinations for the standard deviation of 5K are depicted in Figs. 13 to 15. In these Figures, the initial determination of quantities was obtained using a constant initial guess of 10km/s for the velocity profile and the final determinations

were achieved by applying ultimate estimation for the velocity profile. As shown in Figs. 13 to 15, despite bad initial determinations, reasonably accurate estimates were attained for cold wall heat flux, wall temperature, and surface recession.

4-2- Altitude estimation

In the same manner, as described for the estimation of velocity, the Current section is devoted to the recovering altitude profile of the probe during entry to the earth's atmosphere. A constant initial guess of 100km was used to reconstruct the altitude profile. Addition of error to the input data is analogous to that explained in the previous section except for test case No. 3 in which random errors with maximum values of $\pm 0.01V_{\max}$ ($V_{\max} = 16.5\text{km/s}$ based on Fig. 2) were added to the predetermined velocity profile.

This can be achieved through the use of 64.05m/s as the

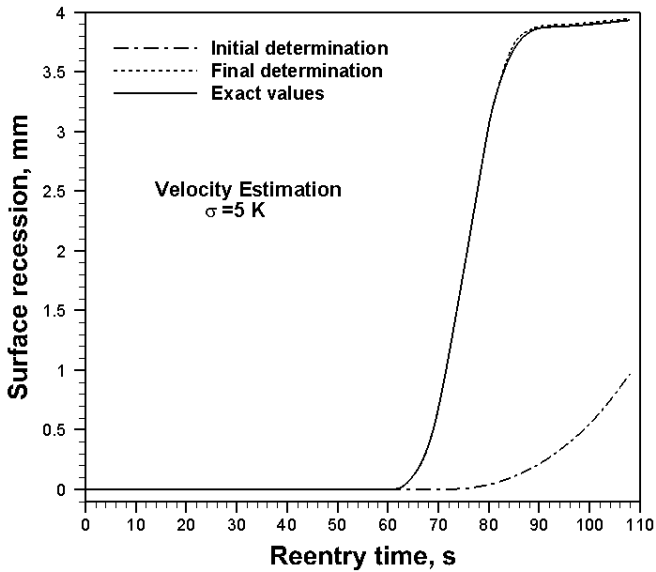


Fig. 15. Initial and ultimate determination of surface recession

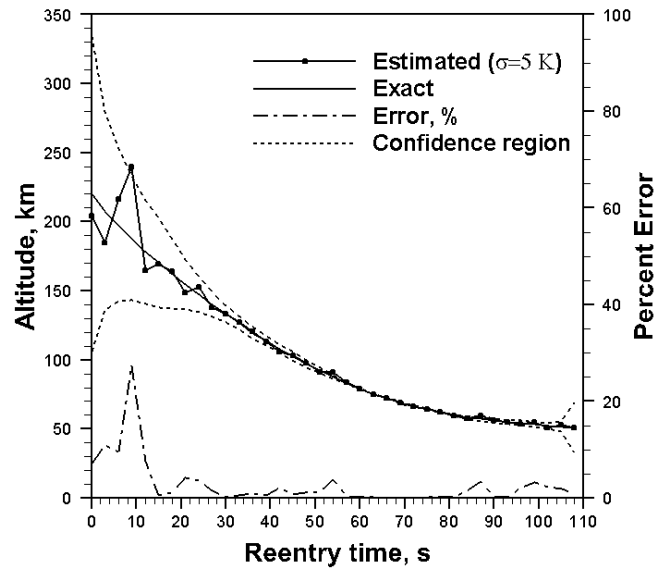


Fig. 17. Retrieved altitude profile using noisy measured temperatures ($\sigma = 5K$)

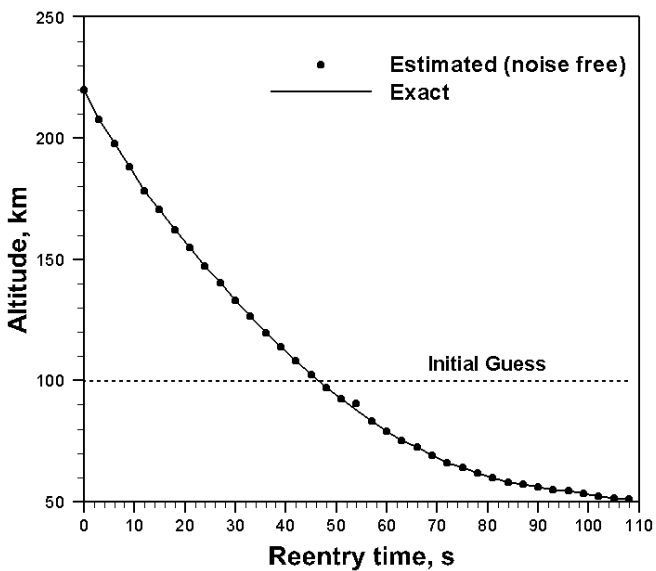


Fig. 16. Recovered altitude profile using noise-free measurements

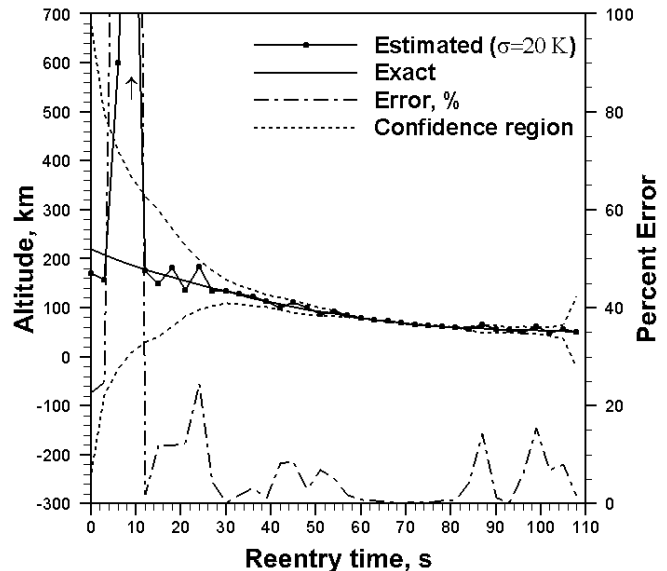


Fig. 18. Retrieved altitude profile using noisy measured temperatures ($\sigma = 20K$)

standard deviation in Eq. (28). The same results, in the same manner, observed in the previous section, were produced regarding altitude estimation of the probe; as can be seen in Figs. 16-23. Some comments can be made about these results as follows: (i) When errorless measured temperatures were used, the adequately precise result was yielded except for estimated altitude at time 54s (Fig. 16). It may be occurred due to forward difference approximation exerted in the current work to compute sensitivity coefficients and thus, using higher-order schemes such as central differencing, although time-consuming, may resolve this inaccuracy issue. (ii) For the cases of noisy measurements, altitude profiles were estimated within the predetermined confidence intervals excluding for some points (Figs. 17 and 18). Regarding the noisy data with a standard deviation of 20K, the retrieved profile of altitude largely deviated from the exact one near the

elapsed entry time of 6s. (iii) Addressing the case in which velocity profile was perturbed by random errors, sufficiently meticulous estimate was achieved for the altitude of the probe (Fig. 19). (iv) Figure 20 exhibits reduction in objective function in analogous treatment to that of Fig. 12 with the discrepancy that larger number of iterations for altitude estimation was required to achieve convergence, as compared to that required for velocity inversion. (v) As shown in Figs. 21-23, notwithstanding the bad initial guess selection for the altitude profile, has led to outlying initial determination for thermal condition and recession of ablating surface, adequately accurate results were eventually anticipated by solving the inverse problem.

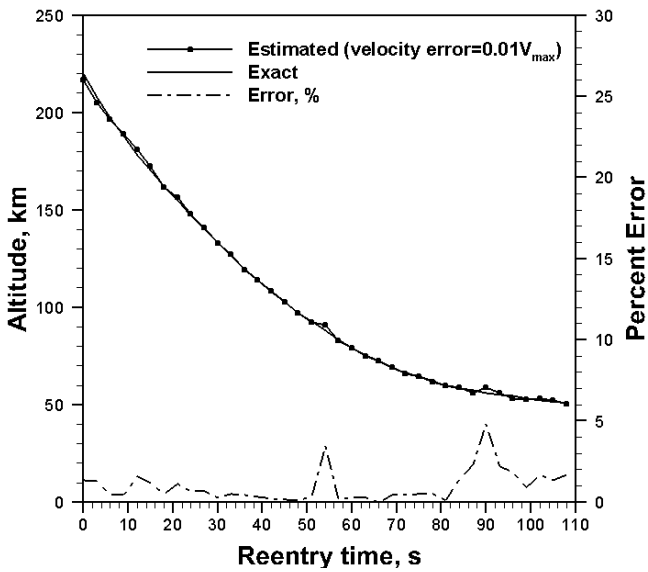


Fig. 19. Retrieved altitude profile using noisy velocity ($\sigma = 64.05\text{m/s}$)

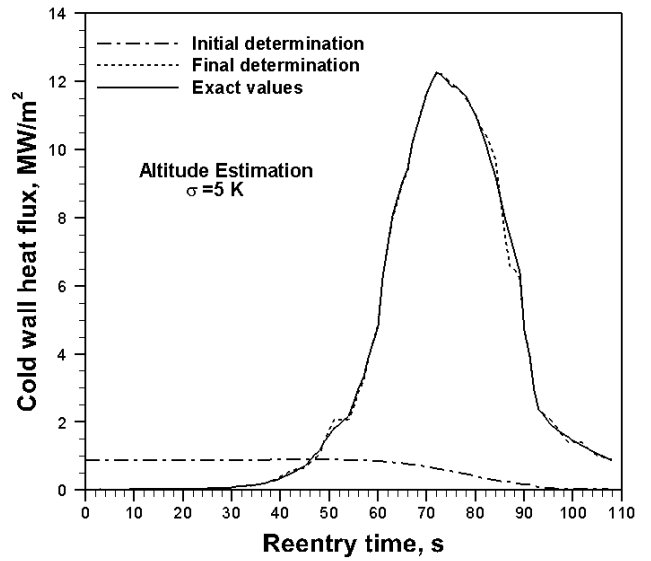


Fig. 21. Initial and ultimate determination of cold wall heat flux

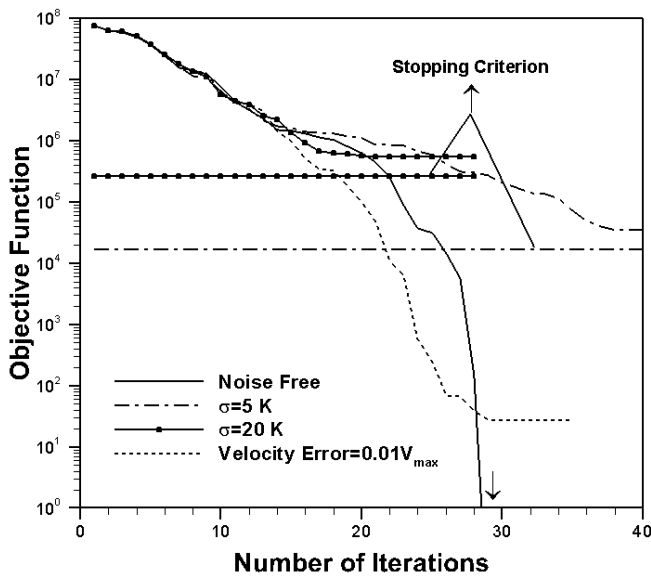


Fig. 20. The values of objective function versus iteration number in case of altitude estimation

4-3- Error analysis

An appropriate benchmark which can be used for error analysis of inverse estimations, is the Normalized Root Mean Square Error (NRMSE) defined as the square root of the time-integrated square of the difference between constituents of exact functions and ultimately estimated ones non-dimensionalized by the time-integrated square of exact profiles. Another criterion used for accuracy assessment of inverse estimations is the Normalized Mean Absolute Error (NMAE), which is the time-averaged difference between exact and predicted parameters normalized by the exact values to make it independent of the unit systems. In mathematical form, these definitions can be expressed by the

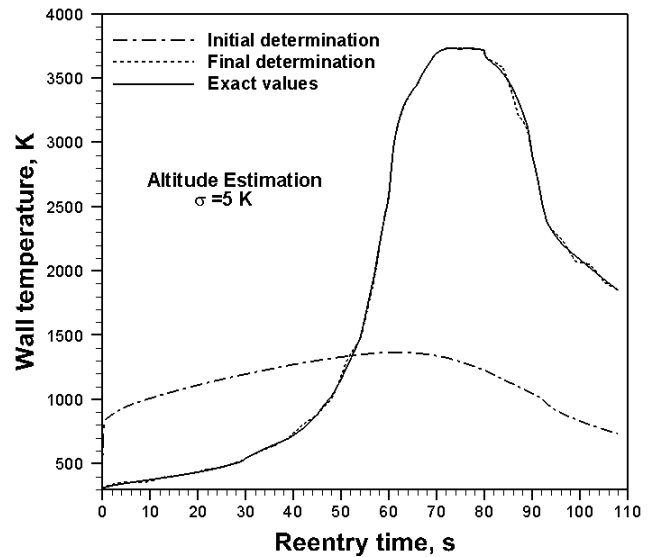


Fig. 22. Initial and ultimate determination of wall temperature

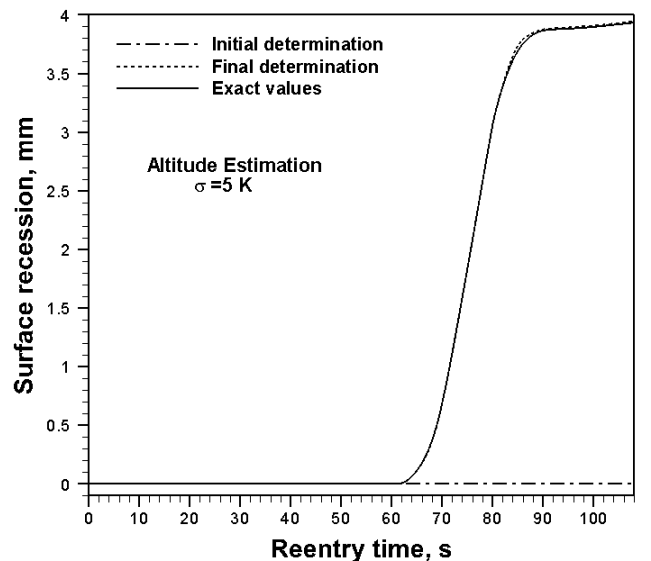


Fig. 23. Initial and ultimate determination of surface recession

Table 1. Results of error calculation for velocity and altitude estimations

Error×100, %	(Noise-free)	$\sigma = 5 \text{ K}$	$\sigma = 20 \text{ K}$	$H_{(err)}=0.01H_{max}$	$V_{(err)}=0.01V_{max}$
Velocity(NRMSE)	4.95×10^{-5}	4.48	21.06	4.14	–
Velocity(NMAE)	2.45×10^{-5}	2.73	11.53	3.70	–
Altitude(NRMSE)	4.44×10^{-1}	10.08	192.11	–	1.19
Altitude(NMAE)	8.78×10^{-2}	2.73	27.90	–	0.95

following relations in order to compute NRMSE and NMAE of estimated functions.

$$X^{NRMSE} = \frac{\sqrt{\frac{1}{T^{final}} \int_0^{T^{final}} \left[X^{(exact)}(t) - X^{(estimated)}(t) \right]^2 dt}}{\frac{1}{T^{final}} \int_0^{T^{final}} |X^{(exact)}(t)| dt} \quad (37)$$

$$X^{NMAE} = \frac{1}{T^{final}} \int_0^{T^{final}} \left| \frac{X^{(exact)}(t) - X^{(estimated)}(t)}{X^{(exact)}(t)} \right| dt \quad (38)$$

where T^{final} represents the final elapsed time of 108s. As can be seen in Table 1, for all cases of noise-free and noisy temperature measurements, velocity estimation was accompanied by less error than altitude estimation. From prior knowledge in the field of the hypersonic phenomena, it was almost predictable that altitude recovering of a hypersonic entry probe at high altitude, in which the air is dilute and aerodynamic heating becomes almost unimportant, will be subjected to the harsh condition. This difficulty led to a large error occurred in the case of altitude estimation regarding noisy measurements with a standard deviation of 20K. On the other hand, estimation of errors using NMAE approach yielded smaller difference between velocity and altitude errors than that of NRMSE relation. Normalized root mean square errors regarding final determination of cold wall heat flux, wall temperature, and surface recession are shown in Table 2. For both cases of velocity and altitude estimations, these errors are in the same order of magnitude, unlike those reported in Table 1. This is due to both the velocity and altitude profiles being accurately recovered in lower elevations (roughly below 100km) and flight trajectory components in this altitude region have more remarkable effects compared to higher altitudes, on the thermal condition of the front-surface of a hypersonic vehicle (e.g., heat flux, wall temperature, and recession), and consequently on the in-depth temperature distribution that the ablative heat shield experienced during entry.

5- Conclusions

The modified Levenberg-Marquardt technique was

Table 2. NRMSE for the final determination of some ablative boundary conditions

Case ($\sigma = 5 \text{ K}$)	Error×100, %		
	q_{cw}	T_w	S
Velocity estimation (NRMSE)	4.07	1.17	0.87
Altitude estimation (NRMSE)	4.21	1.05	0.74

successfully implemented to inversely estimate the flight trajectory of an entry probe. In this regard, four sensors were assumed to be located through-the-thickness of the ablative heat shield to record temperatures. Due to the severe heat load to which the probe was exposed during entry, the three shallower sensors burned out and only the deepest one withstood until the final elapsed time of entry. Pre-statistical analysis showed that the correlation difficulty was drastically decreased by increasing the number of sensors from 1 to 4. As outlined in results, at lower altitudes where the air is dense, estimations of the velocity and altitude were accompanied by more accuracy than those of higher ones. Accordingly, some oscillations appeared in the estimations at early entry times associated with high altitudes, especially for the case of altitude retrieving. In addition to the cases of errorless and noisy temperature measurements, other test cases involving errors in pre-known velocity (in the case of altitude estimation) and altitude (in the case of velocity estimation) were conducted to examine the stability of the current inverse solution with respect to errors in the input data. It was observed that a consistent and highly precise solution was achieved in the presence of pre-determined noisy altitude or velocity.

NOMENCLATURE

A_j	Pre-exponential factor, Eq. (15), s^{-1}	S	Objective function; or surface recession, m
a, b	Radiation exponents, Eq. (10)	\dot{S}	surface recession rate, m/s
B'_c	Normalized ablation rate	T	Temperature, K
B'_g	Normalized flux of pyrolysis gas	t	Time, s
C	Radiation constant, Eq. (10)	u	Velocity, m/s
$cov(X_1, X_2)$	Covariance of X_1 and X_2	x	Coordinate fixed to receding surface

C_p	Specific heat, J/(kg.K)	X	Vector of unknown parameters
E_f/R	Activation energy for decomposition, Eqs. (15), K	Y	Simulated temperature of sensors, K
h_D	Chemical enthalpy, J/kg	Γ	the volume fraction of resin in the virgin composite
H	Enthalpy, J/kg	γ	Specific heat ratio
h_r	Recovery enthalpy, J/kg	ϵ	Tolerance
\bar{h}	enthalpy term defined in Eq. (14), J/kg	μ	Damping parameter in Eq. (19); or viscosity, kg/m.s
J	Number of unknown parameters	ρ	Density, kg/m ³
J	Sensitivity matrix	σ	variance of measurements' error
K	Thermal conductivity, W/(m.K)	σ_x	the variance of error in the estimated parameters
Le	Lewis number	$\phi_{blowing}$	Blowing correction factor
M	Number of sensors; or Mach number	ψ	Diagonal matrix used in LMM
\dot{m}	Mass flux, kg/(m ² .s)	Subscripts	
N	Number of measurements per sensor	B, C	Components of resin
N	Reaction order, Eqs. (15)	D	Reinforcement
P	Pressure, Pa	c	Char
Pr	Prandtl number	e	Edge of boundary layer
q_{cw}	Cold wall heat flux, J/(m ² .s)	g	Pyrolysis gas
q_{rad}	Rate of radiative energy input to the surface, J/(m ² .s)	v	Virgin
R	Recovery factor	w	Wall
R	Nose radius, m	Superscript	
R	Correlation matrix	T	Transpose of a matrix

REFERENCES

[1] O.M. Alifanov, Inverse heat transfer problems, Springer Science & Business Media, 2012.
 [2] J.V. Beck, K.J. Arnold, Parameter estimation in engineering and science, James Beck, 1977.
 [3] M.N. Ozisik, Inverse heat transfer: fundamentals and applications, Routledge, 2018.
 [4] F. Bozzoli, A. Mocerino, S. Rainieri, P. Vocale, Inverse heat transfer modeling applied to the estimation of the apparent thermal conductivity of an intumescent fire retardant paint, Experimental Thermal and Fluid Science, 90 (2018) 143-152.
 [5] C.-W. Chang, C.-H. Liu, C.-C. Wang, Review of computational schemes in inverse heat conduction problems, Smart Science, 6(1) (2018) 94-103.
 [6] O. Fabela, S. Patil, S. Chintamani, B.H. Dennis, Estimation of effective thermal conductivity of porous Media utilizing inverse heat transfer analysis on cylindrical conFigureation, in: ASME 2017 International Mechanical Engineering Congress and Exposition, American Society of Mechanical Engineers Digital Collection, 2017.
 [7] M. Jahedi, F. Berntsson, J. Wren, B. Moshfegh, Transient inverse heat

conduction problem of quenching a hollow cylinder by one row of water jets, International Journal of Heat and Mass Transfer, 117 (2018) 748-756.
 [8] F. Kowsary, A. Behbahaninia, A. Pourshaghagh, Transient heat flux function estimation utilizing the variable metric method, International communications in heat and mass transfer, 33(6) (2006) 800-810.
 [9] T. Loulou, Combined parameter and function estimation with application to thermal conductivity and surface heat flux, Journal of Heat Transfer, 129(10) (2007) 1309-1320.
 [10] M. Mohammadiun, Time-dependent heat flux estimation in multi-layer systems by inverse method, Journal of Thermophysics and Heat Transfer, (null) (2016) 599-607.
 [11] H. Molavi, A. Hakkaki-Fard, R.K. Rahmani, A. Ayasoufi, M. Molavi, A novel methodology for combined parameter and function estimation problems, Journal of Heat Transfer, 132(12) (2010) 121301.
 [12] C.-y. Yang, Estimation of boundary conditions in nonlinear inverse heat conduction problems, Journal of thermophysics and heat transfer, 17(3) (2003) 389-395.
 [13] J. Zueco, F. Alhama, C.G. Fernandez, Numerical nonlinear inverse problem of determining wall heat flux, Heat and mass transfer, 41(5) (2005) 411-418.
 [14] K. Dowding, J. Beck, A. Ulbrich, B. Blackwell, J. Hayes, Estimation of thermal properties and surface heat flux in carbon-carbon composite, Journal of Thermophysics and Heat Transfer, 9(2) (1995) 345-351.
 [15] V. Petrushevsky, S. Cohen, Nonlinear inverse heat conduction with a moving boundary: heat flux and surface recession estimation, (1999).
 [16] A.P. de Oliveira, H.R. Orlande, Estimation of the heat flux at the surface of ablating materials by using temperature and surface position measurements, Inverse Problems in Science and Engineering, 12(5) (2004) 563-577.
 [17] A. Hakkaki-Fard, F. Kowsary, Heat flux estimation in a charring ablator, Numerical Heat Transfer, Part A: Applications, 53(5) (2007) 543-560.
 [18] H.B. Khaniki, S.H. Karimian, Determining the heat flux absorbed by satellite surfaces with temperature data, Journal of Mechanical Science and Technology, 28(6) (2014) 2393-2398.
 [19] H. Mohammadiun, H. Molavi, H.R.T. Bahrami, M. Mohammadiun, Real-Time Evaluation of Severe Heat Load Over Moving Interface of Decomposing Composites, Journal of Heat Transfer, 134(11) (2012) 111202.
 [20] M. Mohammadiun, H. Molavi, H.R.T. Bahrami, H. Mohammadiun, Application of sequential function specification method in heat flux monitoring of receding solid surfaces, Heat Transfer Engineering, 35(10) (2014) 933-941.
 [21] H. Molavi, A. Hakkaki-Fard, M. Molavi, R.K. Rahmani, A. Ayasoufi, S. Noori, Estimation of boundary conditions in the presence of unknown moving boundary caused by ablation, International Journal of Heat and Mass Transfer, 54(5-6) (2011) 1030-1038.
 [22] H. Molavi, I. Pourshaban, A. Hakkaki-Fard, M. Mohlavi, Ablative Materials' Boundary Condition Simulation by Applying Inverse Approach and Euler Solver, Journal of Thermophysics and Heat Transfer, 26(1) (2012) 47-56.
 [23] H. Molavi, R.K. Rahmani, A. Pourshaghagh, E.S. Tashnizi, A. Hakkaki-Fard, Heat flux estimation in a nonlinear inverse heat conduction problem with moving boundary, Journal of Heat Transfer, 132(8) (2010) 081301.
 [24] A. Plotkowski, M.J.M. Krane, The use of inverse heat conduction models for estimation of transient surface heat flux in electroslog remelting, Journal of Heat Transfer, 137(3) (2015) 031301.
 [25] T.-S. Wu, H.-L. Lee, W.-J. Chang, Y.-C. Yang, An inverse hyperbolic heat conduction problem in estimating pulse heat flux with a dual-phase-lag model, International Communications in Heat and Mass Transfer, 60 (2015) 1-8.
 [26] W.D. Henline, M.E. Tauber, Trajectory-based heating analysis for the European Space Agency/Rosetta Earth return vehicle, Journal of Spacecraft and Rockets, 31(3) (1994) 421-428.
 [27] J.A. Fay, F.R. Riddell, Theory of stagnation point heat transfer in dissociated air, Journal of the Aerospace Sciences, 25(2) (1958) 73-85.
 [28] M.E. Tauber, K. Sutton, Stagnation-point radiative heating relations for Earth and Mars entries, Journal of Spacecraft and Rockets, 28(1) (1991) 40-42.

- [29] C.B. Moyer, R.A. Rindal, An analysis of the coupled chemically reacting boundary layer and charring ablator. part 2-finite difference solution for the in-depth response of charring materials considering surface chemical and energy balances, (1968).
- [30] C.F. Hansen, Approximations for the thermodynamic and transport properties of high-temperature air, National Aeronautics and Space Administration, 1959.
- [31] H. Molavi, I. Pourshaban, A. Hakkaki-Fard, M. Molavi, A. Ayasoufi, R.K. Rahmani, Inverse identification of thermal properties of charring ablators, *Numerical Heat Transfer, Part B: Fundamentals*, 56(6) (2010) 478-501.
- [32] R. POTTS, Hybrid integral/quasi-steady solution of charring ablation, in: 5th Joint Thermophysics and Heat Transfer Conference, 1990, pp. 1677.
- [33] S. Williams, D.M. Curry, *Thermal protection materials: thermophysical property data*, (1992).
- [34] V. Tahmasbi, S. Noori, Thermal analysis of honeycomb sandwich panels as substrate of ablative heat shield, *Journal of Thermophysics and Heat Transfer*, 32(1) (2017) 129-140.

HOW TO CITE THIS ARTICLE

Tahmasbi V., Noori S. *Extending Inverse Heat Conduction Method to Estimate Flight Trajectory of a Reentry Capsule. AUT J. Mech Eng.*, 4(4) (2020) 505-522.

DOI: [10.22060/ajme.2020.17000.5845](https://doi.org/10.22060/ajme.2020.17000.5845)



